Enhanced second-harmonic generation from magnetic resonance in AlGaAs nanoantennas

L. Carletti,[1,*] A. Locatelli,[1] O. Stepanenko,[2] G. Leo,[2] and C. De Angelis[1]

[1]*Department of Information Engineering, University of Brescia, Via Branze 38, Brescia 25123, Italy*
[2]*Matériaux et Phénomènes Quantiques, Université Paris Diderot—CNRS, Sorbonne Paris Cité, 10 rue Alice Domon et Léonie Duquet, F-75013 Paris, France*
[*]*luca.carletti@unibs.it*

Abstract: We designed AlGaAs-on-aluminium-oxide all-dielectric nanoantennas with magnetic dipole resonance at near-infrared wavelengths. These devices, shaped as cylinders of 400nm height and different radii, offer a few crucial advantages with respect to the silicon-on-insulator platform for operation around 1.55μm wavelength: absence of two-photon absorption, high $\chi^{(2)}$ nonlinearity, and the perspective of a monolithic integration with a laser. We analyzed volume $\chi^{(2)}$ nonlinear effects associated to a magnetic dipole resonance in these nanoantennas, and we predict second-harmonic generation exceeding 10^{-3} efficiency with 1GW/cm^2 of pump intensity.

OCIS codes: (130.3120) Integrated optics devices; (050.6624) Subwavelength structures; (190.2620) Harmonic generation and mixing.

References and links

1. J. A. Schuller, E. S. Barnard, W. Cai, Y. C. Jun, J. S. White, and M. L. Brongersma, "Plasmonics for extreme light concentration and manipulation," Nat. Mater. **9**(3), 193–204 (2010).
2. B. Sharma, R. R. Frontiera, A.-I. Henry, E. Ringe, and R. P. Van Duyne, "SERS: Materials, applications, and the future," Mater. Today **15**(1-2), 16–25 (2012).
3. A. Kinkhabwala, Z. Yu, S. Fan, Y. Avlasevich, K. Mullen, and E. W. Moerner, "Large single-molecule fluorescence enhancements produced by a bowtie nanoantenna," Nat. Photonics **3**(11), 654–657 (2009).
4. H. A. Atwater and A. Polman, "Plasmonics for improved photovoltaic devices," Nat. Mater. **9**(3), 205–213 (2010).
5. E. Boisselier and D. Astruc, "Gold nanoparticles in nanomedicine: preparations, imaging, diagnostics, therapies and toxicity," Chem. Soc. Rev. **38**(6), 1759–1782 (2009).
6. A. Alù and N. Engheta, "Input impedance, nanocircuit loading, and radiation tuning of optical nanoantennas," Phys. Rev. Lett. **101**(4), 043901 (2008).
7. A. Locatelli, C. De Angelis, D. Modotto, S. Boscolo, F. Sacchetto, M. Midrio, A.-D. Capobianco, F. M. Pigozzo, and C. G. Someda, "Modeling of enhanced field confinement and scattering by optical wire antennas," Opt. Express **17**(19), 16792–16800 (2009).
8. J. C. Ginn, I. Brener, D. W. Peters, J. R. Wendt, J. O. Stevens, P. F. Hines, L. I. Basilio, L. K. Warne, J. F. Ihlefeld, P. G. Clem, and M. B. Sinclair, "Realizing optical magnetism from dielectric metamaterials," Phys. Rev. Lett. **108**(9), 097402 (2012).
9. P. Albella, R. Alcaraz de la Osa, F. Moreno, and S. A. Maier, "Electric and magnetic field enhancement with ultralow heat radiation dielectric nanoantennas: considerations for surface-enhanced spectroscopies," ACS Photonics **1**(6), 524–529 (2014).
10. M. R. Shcherbakov, D. N. Neshev, B. Hopkins, A. S. Shorokhov, I. Staude, E. V. Melik-Gaykazyan, M. Decker, A. A. Ezhov, A. E. Miroshnichenko, I. Brener, A. A. Fedyanin, and Y. S. Kivshar, "Enhanced third-harmonic generation in silicon nanoparticles driven by magnetic response," Nano Lett. **14**(11), 6488–6492 (2014).
11. A. B. Evlyukhin, S. M. Novikov, U. Zywietz, R. L. Eriksen, C. Reinhardt, S. I. Bozhevolnyi, and B. N. Chichkov, "Demonstration of magnetic dipole resonances of dielectric nanospheres in the visible region," Nano Lett. **12**(7), 3749–3755 (2012).
12. S. Person, M. Jain, Z. Lapin, J. J. Sáenz, G. Wicks, and L. Novotny, "Demonstration of zero optical backscattering from single nanoparticles," Nano Lett. **13**(4), 1806–1809 (2013).
13. R. Gómez-Medina, B. García-Cámara, I. Suárez-Lacalle, F. González, F. Moreno, M. Nieto-Vesperinas, and J. J. Sáenz, "Electric and magnetic dipolar response of Germanium spheres: Interference effects, scattering anisotropy and optical forces," J. Nanophotonics **5**(1), 053512 (2011).
14. J. van de Groep and A. Polman, "Designing dielectric resonators on substrates: combining magnetic and electric resonances," Opt. Express **21**(22), 26285–26302 (2013).

#246503 Received 22 Jul 2015; revised 31 Aug 2015; accepted 31 Aug 2015; published 1 Oct 2015

15. I. Staude, A. E. Miroshnichenko, M. Decker, N. T. Fofang, S. Liu, E. Gonzales, J. Dominguez, T. S. Luk, D. N. Neshev, I. Brener, and Y. Kivshar, "Tailoring directional scattering through magnetic and electric resonances in subwavelength silicon nanodisks," ACS Nano **7**(9), 7824–7832 (2013).
16. A. Rose, D. Huang, and D. R. Smith, "Nonlinear interference and unidirectional wave mixing in metamaterials," Phys. Rev. Lett. **110**(6), 063901 (2013).
17. M. R. Shcherbakov, A. S. Shorokhov, D. N. Neshev, B. Hopkins, I. Staude, E. V. Melik-Gaykazyan, A. a. Ezhov, A. E. Miroshnichenko, I. Brener, A. a. Fedyanin, and Y. S. Kivshar, "Nonlinear interference and tailorable third-harmonic generation from dielectric oligomers," ACS Photonics **2**, 578-582 (2015).
18. S. Gehrsitz, F. K. Reinhart, C. Gourgon, N. Herres, A. Vonlanthen, and H. Sigg, "The refractive index of AlxGa1−xAs below the band gap: accurate determination and empirical modeling," J. Appl. Phys. **87**(11), 7825–7837 (2000).
19. P. Grahn, A. Shevchenko, and M. Kaivola, "Electromagnetic multipole theory for optical nanomaterials," New J. Phys. **14**(9), 093033 (2012).
20. M. Kauranen and A. V. Zayats, "Nonlinear Plasmonics," Nat. Photonics **6**(11), 737–748 (2012).
21. D. de Ceglia, M. A. Vincenti, C. De Angelis, A. Locatelli, J. W. Haus, and M. Scalora, "Role of antenna modes and field enhancement in second harmonic generation from dipole nanoantennas," Opt. Express **23**(2), 1715–1729 (2015).
22. M. Celebrano, X. Wu, M. Baselli, S. Großmann, P. Biagioni, A. Locatelli, C. De Angelis, G. Cerullo, R. Osellame, B. Hecht, L. Duò, F. Ciccacci, and M. Finazzi, "Mode matching in multiresonant plasmonic nanoantennas for enhanced second harmonic generation," Nat. Nanotechnol. **10**(5), 412–417 (2015).
23. S. S. Kruk, M. Weismann, A. Bykov, E. Mamonov, I. Kolmychek, T. Murzina, N. Panoiu, D. N. Neshev, and Y. S. Kivshar, "Enhanced magnetic second-harmonic generation from resonant metasurfaces," ACS Photonics **2**(8), 1007–1012 (2015).
24. Z. Yang, P. Chak, A. D. Bristow, H. M. van Driel, R. Iyer, J. S. Aitchison, A. L. Smirl, and J. E. Sipe, "Enhanced second-harmonic generation in AlGaAs microring resonators," Opt. Lett. **32**(7), 826–828 (2007).

1. Introduction

Optical nanoantennas are nanoscale structures capable of efficiently collecting free-space light and confining it into subwavelength volumes far below the diffraction limit [1]. This unusual optical capability to strongly manipulate light at the nanoscale has proven useful for a huge range of applications such as surface enhanced Raman scattering [2], surface enhanced fluorescence [3], solar cells [4], nanomedicine [5]. The nanoantennas used in those demonstrations were made of nanometallic objects. Their optical properties, based on plasmonic resonances, can be predicted using design guidelines which have been developed starting from well-established techniques already in use at microwave frequencies [6,7]. Even though plasmonic antennas have been employed for many applications, metals suffer from large resistive heating losses in the visible and near-infrared (near-IR) wavelength range, which limit device performance [8,9]. Therefore, several recent works [8–13] have focused on a new class of all-dielectric optical nanoantennas. These consist of high-permittivity low-loss dielectric particles of sub-micrometer size. In contrast to plasmonic antennas, the optical response of dielectric particles does not suffer from ohmic losses and can exhibit both strong electric and magnetic optical resonances at visible or near-IR wavelengths [11,12].

Semiconductor nanoparticles are emerging as a promising alternative to metallic ones for a wide range of nanophotonic applications based on localized resonant modes in the entire visible and near-IR spectral ranges, see e.g [8–10]. Different particle geometries can be considered, but mainly spherical and cylindrical antennas have been dealt with to date. Nanodisks have recently proven versatile in tailoring of electric and magnetic response, stemming from two degrees of freedom: radius and height [14,15]. Also, as opposed to nanospheres, the fabrication of nanodisks is easily accessed by modern electron beam lithography, which enables a precise control of the nanodisk size and lattice geometries.

Dielectric nanostructures on a low-index substrate have been recently demonstrated in the framework of semiconductor planar technology, encompassing the cases of silicon on insulator [10], as well as GaAs on silica [12]. All-dielectric nanoantennas offer unique opportunities for the study of nonlinear effects due to very low losses in combination with multipolar characteristics of both electric and magnetic resonant optical modes [10]. The nonlinear optical effects of magnetic origin can have fundamentally different properties compared with those of electric origin. When nonlinearities of both electric and magnetic type are present, the nonlinear response can be substantially modified and is accompanied by nonlinear mode mixing and magnetoelectric coupling [16,17]. To the best of our knowledge,

#246503 Received 22 Jul 2015; revised 31 Aug 2015; accepted 31 Aug 2015; published 1 Oct 2015

the only investigations of the nonlinear optical response generated from a magnetic resonant optical mode in an all-dielectric antenna have been conducted on Si nanodisks [10,14]. However, in that case, operation in the third window of optical fiber communication is limited by two-photon absorption (TPA) and volume $\chi^{(2)}$ interactions are absent because of centro-symmetry of Si. In this perspective III-V materials such as GaAs or AlGaAs offer a strong potential to efficiently observe second order nonlinear effects such as Second-Harmonic Generation (SHG). Furthermore, by engineering the AlGaAs alloy composition, TPA at wavelengths close to 1.55μm can be avoided. Finally, at variance with indirect-bandgap Si, AlGaAs monolithic nanoantennas might benefit from the direct integration of diode lasers on a GaAs chip.

For all these reasons, here we study the linear and nonlinear scattering of AlGaAs-on-aluminum-oxide monolithic nanodisks. In Section 2, we illustrate the design of nanodisks exhibiting the magnetic dipole (MD) resonance in the near-IR wavelength range. In Section 3, we report, for the first time, an analysis of the optical nonlinear response generated from volume $\chi^{(2)}$ nonlinearity in all-dielectric nanodisks. Our results show that AlGaAs nanoantennas have a strong potential to enhance the SHG from all-dielectric nanostructures.

2. Design of AlGaAs nanoantennas

We investigated the scattering characteristics of $Al_{0.18}Ga_{0.82}As$ cylinders at near-IR wavelengths by using finite element method simulations in COMSOL. As shown in the inset of Fig. 1(a), the incident light was a plane wave with a wave vector, **k**, parallel to the cylinder axis and the electric field, **E**, polarized along the x-axis.

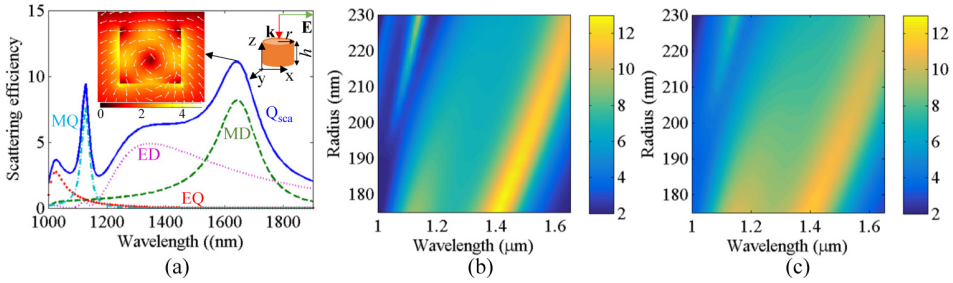

Fig. 1. (a) Scattering efficiency Q_{sca}, decomposed in magnetic dipole (MD), electric dipole (ED), magnetic quadrupole (MQ), and electric quadrupole (EQ) contributions, as a function of wavelength calculated for r = 225 nm and h = 400 nm. A schematics of the AlGaAs cylinder with the incident field and the cross section of normalized |(**E**)| in the x-z plane through the axis of the cylinder are shown in the inset. The arrows represent (**E**) in the same x-z plane. (b) and (c) scattering efficiency as a function of wavelength and cylinder radius for a constant height h = 400 nm for cylinders suspended in air and on a substrate with n = 1.6 respectively.

For the dispersion of the refractive index of $Al_{0.18}Ga_{0.82}As$ we used the analytical model proposed in [18] which was derived from comparison with measurements. The scattering efficiency (defined as $Q_{sca} = C_{sca}/\pi r^2$ where C_{sca} is the scattering cross-section and r is the cylinder radius) calculated for a cylinder suspended in air with radius r = 225 nm and height h = 400 nm is shown in Fig. 1(a). The multipole expansion of Q_{sca}, calculated by applying the method in [19], is also shown in Fig. 1(a). We can observe that several resonant peaks appear at wavelengths shorter than about λ = 1700 nm while, for longer wavelengths, the scattering efficiency monotonically decreases. In particular, the sharper and strongest resonance observed at λ = 1640 nm is mainly due to a MD resonance, as it can be inferred from the field distribution shown in the inset of Fig. 1(a) [11]. Because the incident electric field was x-polarized, the main components of the electric field inside the cylinder are along the x and z directions. The broader resonance at λ = 1300 nm is of electric dipole type while higher-order multipoles contribute to the resonances observed at shorter wavelengths (see Fig. 1(a)). When the geometric parameters of the antenna are changed, the resonances observed in Fig. 1(a)

#246503 Received 22 Jul 2015; revised 31 Aug 2015; accepted 31 Aug 2015; published 1 Oct 2015

shift in wavelength. The scattering efficiency of cylinders with radius varying from 175 nm up to 230 nm and a constant height of 400 nm is shown in Fig. 1(b). It can be seen that the resonant peaks mainly red-shift as the radius of the cylinder is increased. For example, the MD resonance peak wavelength shifts from λ = 1410 nm when r = 175 nm up to λ = 1655 nm when r = 230 nm. The scattering efficiency for the same cylinders, but on a substrate with a refractive index of 1.6, is shown in Fig. 1(c). This configuration reflects the case of the antennas fabricated onto an aluminum oxide substrate. We can see that the effect of the substrate on the scattering efficiency is small (e.g. for r = 220 nm the MD resonance wavelength is about 1620 nm in the case without the substrate and 1630 nm with the substrate). The presence of the substrate does not radically alter the scattering efficiency of the cylinder because of the large difference between the refractive index of the AlGaAs nanodisk and the aluminum oxide substrate that can be obtained in the AlGaAs-on-aluminum-oxide material platform.

3. Second-Harmonic Generation in AlGaAs nanoantennas

Second harmonic generation in plasmonic nanostructures has been deeply investigated in recent years, often enhanced by matching localised surface plasmon resonance (LSPR) either with the excitation or the emission wavelength [20–22]. Furthermore, SHG from metal-dielectric-metal metasurfaces has been studied [23]. In all these cases the main contribution to the second harmonic (SH) signal came from the surface nonlinearity of the metal while the volume contribution was negligible. In this work, since AlGaAs is a non-centrosymmetric material, we have a strong volume contribution which could enhance the SH signal. We first note that, among the different resonant modes that have been observed in the nanodisks, for example in Fig. 1(a), the MD resonance shows the strongest scattering efficiency. This can potentially enhance the nonlinear optical response achievable from these nanoantennas. Moreover, the only non-zero elements of the second order nonlinear susceptibility $\chi_{ijk}^{(2)}$ of $Al_{0.18}Ga_{0.82}As$ oriented along the [$\bar{1}00$] crystalline axis have $i \neq j \neq k$ [24].

In order to illustrate the potential of AlGaAs cylinders for nonlinear nanophotonics, we investigated the SHG phenomenon by using the nonlinear polarization induced by $\chi^{(2)}$ as a source in COMSOL simulations. We define the SHG efficiency as

$$\eta_{SHG} = \frac{\int_A \vec{S}_{SH} \cdot \hat{n}\, da}{I_0 \times \pi r^2} \tag{1}$$

where $\vec{S}_{SH}$ is the Poynting vector of the SH field, $\hat{n}$ is the unit vector normal to a surface A enclosing the antenna, and I_0 is the incident field intensity (I_0 = 1 GW/cm^2 in the simulations). The calculated SHG efficiency for a cylinder with r = 225 nm and h = 400 nm suspended in air is shown in Fig. 2(a). In the calculations, we used $\chi^{(2)}$ = 100 pm/V as reported for $Al_{0.18}Ga_{0.82}As$ in [24]. As it can be seen, the maximum SHG efficiency is obtained for a pump wavelength of λ = 1675 nm, which is close to the MD resonance wavelength (i.e. λ = 1640 nm, see Fig. 1(a)).

One would normally expect to observe the strongest enhancement of the SHG when pumping at the MD resonance. Therefore, in order to understand why the maximum of η_{SHG} was not obtained for a pumping wavelength of λ = 1640 nm, we calculated the linear scattering efficiency for wavelengths between 785 nm and 900 nm (shown in Fig. 2(b)). We can observe that there is a resonance at λ = 837.5 nm that can explain the SHG efficiency enhancement when pumping at λ = 1675 nm. Another resonance is found at λ = 820 nm, that is exactly at half the MD resonance peak. However, the SHG efficiency using a pump wavelength of 1640 nm (thus matching the MD resonance) is smaller than the one obtained with a pump wavelength of 1675 nm. In order to clarify this point, we evaluated the overlap integral defined as

#246503 Received 22 Jul 2015; revised 31 Aug 2015; accepted 31 Aug 2015; published 1 Oct 2015

$$\zeta = \frac{\left| \int E_x^{FF} E_z^{FF} \left(E_y^{SH} \right)^* dV \right|}{\sqrt{\int \left| E_x^{FF} E_z^{FF} \right|^2 dV} \sqrt{\int \left| E_y^{SH} \right|^2 dV}} \tag{2}$$

where E_i^{FF} and E_i^{SH} are the components of the electric field along the *i*-axis for the pump and the emission, or SH, modes, respectively. In the overlap integral we considered only this combination of fields because of two reasons. First, the main components of the electric field at the MD resonance are those in the *x* and *z* axis. Second, the only non-zero terms of the second order nonlinear susceptibility are those with $i \neq j \neq k$. The overlap integral between the mode at λ = 820 nm and the mode at the pump wavelength of 1640 nm is only about 14%, whereas ζ is about 54% between the modes at λ = 837.5 nm and λ = 1675 nm (i.e. where the maximum of η_{SHG} is observed, see Fig. 2(a)). Therefore, since the MD resonance is spectrally broader than the resonances in the wavelength range corresponding to the SH signal, the SHG efficiency depends strongly on the overlap between the modes at the emission and pump wavelength. The magnitude of the electric field of the SH signal generated with a pump at λ = 1675 nm is shown in the inset of Fig. 2(a). The far-field radiation pattern is shown in Fig. 3(c) and we can recognize a quadrupolar emission pattern.

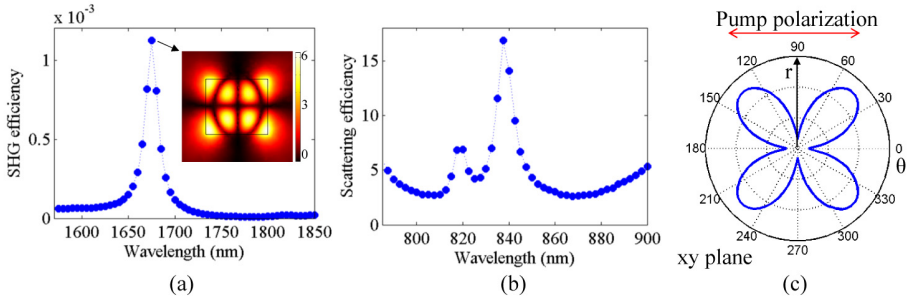

Fig. 2. (a) SHG efficiency as a function of pump wavelength for a cylinder with *r* = 225 nm, *h* = 400nm suspended in air and pump intensity I_0 = 1GW/cm^2. The normalized $|(\mathbf{E})^{SH}|$ on a cross section in the x-z plane at the center of the cylinder is shown in the inset. (b) Scattering efficiency at wavelengths between 785 nm and 900 nm. (c) Far-field radiation pattern of the SH electric field in the x-y plane.

Figure 3(a) provides the SHG efficiency as a function of pump wavelength and cylinder radius. The peak wavelength of SHG efficiency redshifts as *r* is increased, following the resonant mode at the emission wavelength that was found to have a good overlap with the MD resonance. The maximum SHG efficiency as a function of the cylinder radius is extracted along the red-dotted line of Fig. 3(a) and shown in Fig. 3(b). We can observe that the wavelength at which the SH signal is generated varies from 788 nm to 848 nm as *r* is varied between 202 nm and 235 nm. Furthermore, we can observe that the SHG efficiency varies only of about 10% in the same range of radii, which might be due to the fact that the MD resonance is spectrally broader than the SH resonance (compare Fig. 1(a) and Fig. 2(b)).

As it can be seen in Fig. 3(b), η_{SHG} initially increases as the cylinder radius is increased and, after a maximum when *r* = 225 nm, it decreases. This behavior can be intuitively explained by evaluating $\upsilon = (Q_{FF})^2 \times Q_{SH} \times \zeta$, where Q_{FF} and Q_{SH} are the scattering efficiency of the pump and second-harmonic modes respectively. The conversion efficiency is expected to increase as Q_{FF}^2 because the intensity of the SH signal scales as the squared power of the electric field intensity of the pump beam. Indeed, if we evaluate υ for the cylinder with *r* = 225nm, we obtain a maximum at λ = 1675 nm, in good agreement with the results shown in Fig. 2(a). When the radius is varied, ζ remains almost constant while the spectral distance between the pump wavelength for which η_{SHG} is maximum and the MD resonance increases (see dotted lines in Fig. 3(a)). Therefore Q_{FF} diminishes which in turn lowers υ, in good agreement with the results shown in Fig. 3(b). Furthermore, we analyzed the SHG efficiency

#246503 Received 22 Jul 2015; revised 31 Aug 2015; accepted 31 Aug 2015; published 1 Oct 2015

for cylinders with different heights (between 300nm and 600nm). We observe that the overlap integral ζ between the pump and the SH mode remains almost unchanged as the height is varied. When the height of the cylinder is decreased, the spectral distance between the SH mode and the MD mode increases. Thus, the maximum of η_{SHG} decreases because the product $(Q_{FF})^2 \times Q_{SH}$ decreases. When the cylinder height is increased, the spectral distance between the pump and the MD mode progressively decreases and the pump wavelength can eventually coincide with the MD resonance for h = 600 nm and r = 300 nm. Despite this fact, we observed that the maximum SHG efficiency is smaller than the one obtained for the cylinder with h = 400 nm. In fact, when the height of the cylinder is increased, Q_{SH} decreases and thus υ decreases as well. From these observations, it is straightforward to understand that in order to maximize η_{SHG}, the nanoparticle geometry should be engineered for, from one side, guaranteeing a fair tradeoff between the need of a high Q_{FF} and a high Q_{SH} to maximize the product $(Q_{FF})^2 \times Q_{SH}$ and, from the other side, optimizing the spatial overlap ζ of the nanoparticle mode at the SH wavelength with the pump mode.

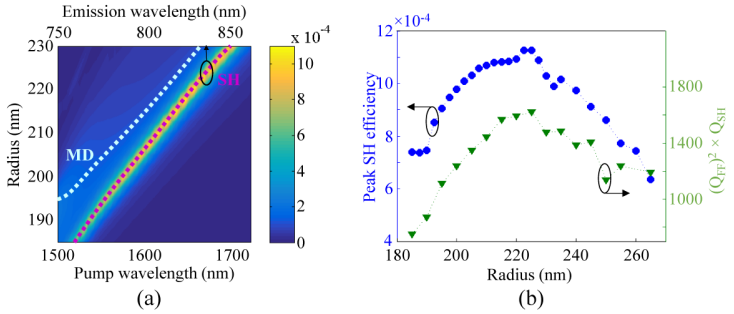

Fig. 3. (a) SHG efficiency as a function of pump wavelength and nanodisk radius. The magnetic dipole resonance (MD) and the resonant mode at the emission wavelength (SH) are outlined with a dotted white and magenta line respectively. (b) Maximum SHG efficiency (circles) and $(Q_{FF})^2 \times Q_{SH}$ (triangles) as a function of nanodisk radius. The nanodisks have constant height of 400 nm and are suspended in air. The pump intensity is 1GW/cm^2.

5. Conclusion

We reported the design AlGaAs on aluminum-oxide nanoantennas. We showed that by varying height and radius of the nanodisk we could obtain a strong MD resonance in the near-IR wavelength range. The SHG phenomenon when the pump wavelength is chosen close to the MD mode was studied. We found that in order to achieve a strong enhancement of the conversion efficiency it is necessary to have a good mode overlap and a strong scattering efficiency of both the pump and the SH mode. These characteristics allowed to predict a SHG efficiency larger than 10^{-3} from a single nanodisk with r = 225nm and h = 400nm and using a pump intensity of I_0 = 1GW/cm^2 at a wavelength of 1675 nm. These antennas can be fabricated using the AlGaAs-on-aluminum-oxide material platform. Our material choice can be advantageous under several perspectives. As far as the nonlinear optical properties are concerned, AlGaAs is a highly nonlinear material with both $\chi^{(2)}$ and $\chi^{(3)}$ nonlinearities and TPA can be avoided at near-IR wavelengths by engineering the alloy composition. Furthermore, the maturity of this III-V material platform can be exploited to realize monolithically integrated devices with, for instance, integrated laser source on chip.

This work is the first investigation of volume second-order nonlinear optical interactions generated from a MD resonance in all-dielectric nanoantennas. Our results show that nanoantennas based on the AlGaAs-on-aluminum-oxide material platform may have a huge potential for applications such as molecular sensing [9] and single biomolecule tracking microscopy [10].

#246503 Received 22 Jul 2015; revised 31 Aug 2015; accepted 31 Aug 2015; published 1 Oct 2015

Acknowledgments

The paper and the participation of all the authors has been made in the framework of the Erasmus Mundus NANOPHI project. L. Carletti, C. De Angelis and A. Locatelli acknowledge financial support from U.S. Army ("Engineering second order nonlinear effects in optical antennas") and CARIPLO ("SHAPES - Second-HArmonic Plasmon-Enhanced Sensing"). G. Leo and Q. Stepanenko acknowledge financial support from the DOLPHIN project of the SEAM (Science and Engineering of Advanced Materials and Devices) Labex of Sorbonne Paris Cité.

#246503 Received 22 Jul 2015; revised 31 Aug 2015; accepted 31 Aug 2015; published 1 Oct 2015